Optical degradation of inductively-coupled plasma lenses by conversion of electromagnetic energy into unsteady flows

By J. Urzay, M. Mortazavi AND A. Mani

1. Motivation and objective

This study addresses the onset of convection in an inductively-coupled model plasma lens. The principle of operation of a plasma lens consists of focusing light by tuning the refractive-index distribution, or equivalently, the electron-density field in a partially-ionized gas environment. Departures from axisymmetry in the electron-density distribution are observed in the present three-dimensional calculations, which imply the existence of underlying dynamics of plasma destabilization. Two mechanisms that lead to plasma motion in the lens are studied, namely, gravity-driven thermal convection, and cycle-averaged Lorentz forcing. In turn, it is observed here that the development of motion in the plasma has important implications for the optical performance of the lens.

2. Background

Solid-state lenses and mirrors have long been used to focus light and cancel aberrations mechanically. However, in some applications such as high-speed aerodynamics and air-to-ground reconnaissance from airplanes, fast steering capabilities are required from the lens to dynamically cancel the high-frequency optical distortions caused by the surrounding air, which is typically in rapid turbulent motion (Wang *et al.* 2012). In addition to increasing several orders of magnitude the damage thresholds over solid-state lenses, the utilization of controllable media in lenses, such as gases or plasmas, warrants enhanced capabilities for prompt optical adaptation (Neiswander *et al.* 2012).

A ray of light traveling through plasma can be bent because of the effects of electrons on the refractive index n. In particular, for light frequencies much larger than the collision frequency, and for sufficiently ionized plasmas, the refractive index in the plasma can be expressed as

$$n^2 = 1 - (\omega_p/\omega_\ell)^2 \tag{2.1}$$

(Fridman & Kennedy 2011), where ω_ℓ is the frequency of the incident ray of light, and $\omega_p = (n^- e^2/\varepsilon_0 m^-)^{1/2}$ is the plasma frequency. In this formulation, e is the proton charge, ε_0 is the permittivity of vacuum, m^- is the electron mass, and n^- is the electron number-density. In this way, the refractive index and the electron density are intimately linked.

For $\omega_\ell < \omega_p$, the plasma has the ability to shield and dissipate the incident radiation by reconfiguring the charges on its outer shell in a regime which is not practically relevant for the purposes of this study. Conversely, for $\omega_\ell > \omega_p$, variations in the refractive index occur due to the presence of electrons, which increase the phase velocity and shorten the path of the light rays as they propagate through the plasma. In this regime, the plasma acts as an effective lens as long as the electrons are coherently distributed within the

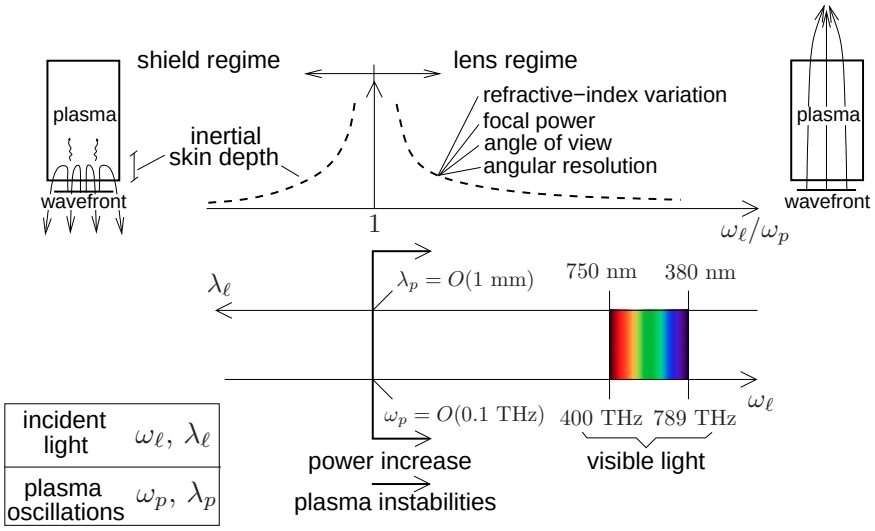

FIGURE 1. Sketch of the overarching problem. Conditions quoted for the plasma frequency ω_p correspond to the-high power (40 kW) mid-pressure (2.2 bar) regime analyzed in this study.

skin depth, which is a layer close to the outer shell where the electromagnetic energy is predominantly deposited and sustains the plasma. In practical applications, ω_p is set by the operating conditions of the plasma, which are typically specified in terms of electric power and pressure. For a given value of ω_p, focusing light of increasingly smaller wavelengths becomes progressively more impractical, since the focal power decreases with increasing values of ω_ℓ/ω_p. An alternative solution for focusing light near the visible range is to increase the plasma frequency. This design shift requires, for instance, the utilization of larger electric powers. However, as shown in this study, high electric powers lead to plasma destabilization and optical degradation of the lens. A regime diagram that considers these processes is depicted in Figure 1.

The model plasma lens considered in this study is sketched in Figure 2. A cylindrical coordinate system $\{r, \theta, z\}$ is used in the formulation. The lens consists of a closed cylinder of radius R and length L filled with Argon (Ar) plasma at pressure p_0 and temperature T_0. The energy is deposited in the plasma by means of electromagnetic coupling between the electrons and the enveloping coil, through which an alternate current is passed at an angular frequency ω_{IN} in the radio-frequency range. In this way, rapidly oscillating magnetic $\mathbf{B}_{\text{IN}}$ and electric $\mathbf{E}_{\text{IN}}$ fields are generated in the cylinder, which energize the plasma. In this notation, boldface symbols denote vector quantities, and the superindices $^+$ and $^-$ represent quantities for ions (Ar^+) and electrons (e^-), respectively. The gravitational acceleration vector $\mathbf{g}$ is assumed to form a constant angle φ with the cylinder axis, which is fixed to $\varphi = 0$ in this study.

The remainder of this report is organized as follows. In Section 2, relevant characteristic scales and nondimensional parameters are obtained that may promote the onset of flow instabilities in the lens as the electric power is increased. In Section 3, the conservation equations of the plasma motion are outlined together with appropriate boundary and initial conditions. In Section 4, the plasma flow field obtained from the numerical integrations is characterized for high-power intakes. Section 5 is focused on the optical performance of the plasma lens. Finally, some brief conclusions are drawn in Section 6.

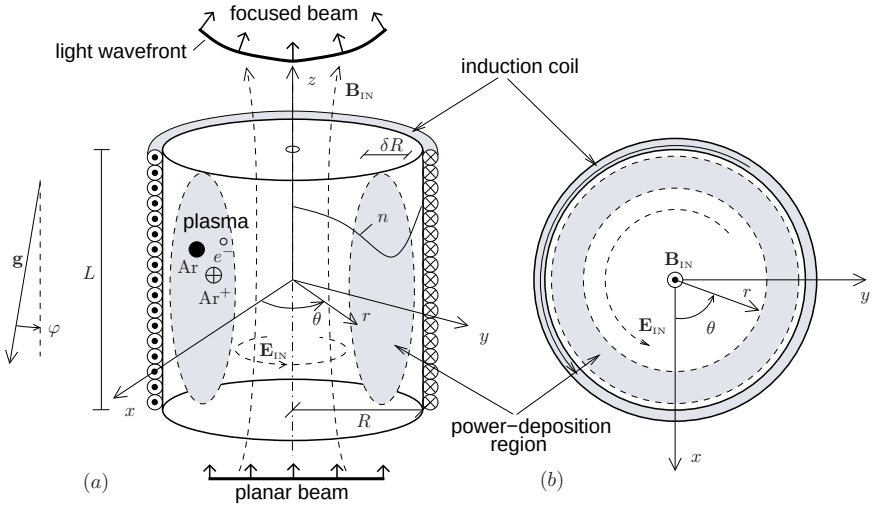

FIGURE 2. Sketch of the model plasma lens. (a) Three-dimensional and (b) in-plane views of the lens geometry. The remaining symbols are defined in the main text.

3. Characteristic scales

The plasma considered here consists of perfect monoatomic gases in local thermodynamic equilibrium. The characteristic time scales for viscous diffusion and heat conduction through the plasma skin region are denoted by $t_\nu = (\delta R)^2/\nu_0$ and $t_T = t_\nu \,\text{Pr}$, where ν_0 is the kinematic viscosity at the reference temperature T_0, Pr is the Prandtl number, and δ is the skin depth nondimensionalized with R, which is introduced below.

3.1. *Electromagnetic and chemical scales*

A time-varying, mostly axial magnetic field of zero mean and characteristic root mean-square value $B_{\text{IN}} = \{\dot{W}_{\text{IN}}/[2\pi L\delta^3 R^4 \sigma_0 \omega_{\text{IN}}^2)\}^{1/2}$ develops upon energizing the coil, where $\dot{W}_{\text{IN}}$ is the electric power dissipated in the plasma, and σ_0 is the typical value of the plasma conductivity. The magnetic field B_{IN} oscillates with a period proportional to the inverse of the induction frequency $t_{\text{IN}} = 2\pi/\omega_{\text{IN}}$ and induces an electric field of order $E_{\text{IN}} = \omega_{\text{IN}}\delta R B_{\text{IN}}$ as indicated by the Faraday's law. The scales $\dot{W}_{\text{IN}}$ and E_{IN} are related as $\dot{W}_{\text{IN}} = 2\sigma_0 E_{\text{IN}}^2 \pi\delta R^2 L$ by the requirement that the deposited electric energy equals the Ohmic dissipation in the plasma skin region.

The charged particles in the plasma move with characteristic cyclotron periods $t_b^- = 2\pi/\omega_b^-$ and $t_b^+ = t_b^-/\mathcal{M}$, where $\omega_b^- = eB_{\text{IN}}/m^-$ is the cyclotron frequency of the electrons. Here,

$$\mathcal{M} = m^-/m \ll 1 \tag{3.1}$$

is the ratio of the atomic masses of electrons to neutrals, with $\mathcal{M} = O(10^{-5})$ in the present application. For the conditions analyzed here, the Hall parameters of the charged particles, $\beta^- = t_c^-/t_b^-$ and $\beta^+ = \mathcal{M}^{1/2}\beta^-$, are small compared to unity. In this formulation, $t_c^- = 1/\mathcal{V}_0^-$ and $t_c^+ = t_c^-/\mathcal{M}^{1/2}$ are, respectively, the typical time scales of collisions of electrons against neutrals (with $\mathcal{V}_0^-$ the corresponding collision frequency defined below), and of ions against neutrals. Specifically, the values $\beta^- = O(10^{-3}) \ll 1$ and $\beta^+ = O(10^{-5}) \ll 1$ are found in the present problem, and therefore the magnetization effects on the transport of charged particles and on the plasma conductivity are

Reaction	A	T_a	b
ionization (i)	$1.2 \cdot 10^{-7*}$	18.7^*	0^*
recombination (r)	$3.8 \cdot 10^{-9\dagger}$	$0^\dagger$	$-4.5^\dagger$

$$e^- + \mathrm{Ar} \underset{r}{\overset{i}{\rightleftharpoons}} \mathrm{Ar}^+ + e^- + e^-$$

TABLE 1. Short description of Argon ionization-recombination chemistry and the corresponding rate parameters, with $k = A(T^-)^b \exp(-T_a/T^-)$ in $\mathrm{cm}^3\mathrm{s}^{-1}\mathrm{particle}^{-1}$ (for k_i) or $\mathrm{cm}^6\mathrm{s}^{-1}\mathrm{particle}^{-2}$ (for k_r), and T_a in eV. Refs.: (*) Bukowski & Graves (1996), (†) Stevefelt *et al.* (1975).

negligible. However, the cumulative effects of the magnetic field are still important in the plasma motion, in that the cycle-averaged Lorentz force caused by the incident electromagnetic field generates a mean electron drift which is an important mechanism for momentum transfer to the plasma in long time scales, as shown below.

The AC electric field E_{IN} induces a fast oscillatory translational motion on the electrons. Since $t_{\mathrm{IN}}/t_c^- \gg 1$, this motion becomes rapidly dominated by collisions after short distances of the order of the electron mean free path λ_0^-, which here is much smaller than the chamber size. In particular, $\mathrm{Kn}^- = \lambda_0^-/R = O(10^{-6}) \ll 1$ represents a typical value of the Knudsen number in this study. In this limit, the plasma conductivity attains collision-limited values of order $\sigma_0 = n_0^- e^2 t_c^-/m^-$, where n_0^- is the characteristic electron number-density.

During the oscillatory motions described above, some of the electrons collide with Ar atoms and ionize them to Ar^+ in accordance with the forward reaction (i) in Table 1. This ionization process occurs in chemical time scales of order $t_i = m/(k_{i,0}\rho_0)$, where $\rho_0 = p_0 m/(k_{\mathrm{B}} T_0)$ is the characteristic density of the plasma, k_{B} is the Boltzmann constant, and $k_{i,0} = A_i \exp(-T_{A,i}/T_0^-)$ is the ionization rate constant based on the characteristic electron temperature T_0^-. The electrons produced from ionization collide with other neutrals generating one electron per collision. In static conditions, this autocatalytic process continues until an equilibrium number-density of electrons n_0^- is reached when the rate of release of new electrons by collisions is balanced with the rate of bulk recombination and wall losses, the former being represented by the backward reaction (r) in Table 1, and the latter being accounted for in a wall boundary condition. Recombination in the bulk becomes more important than on walls for establishing an equilibrium concentration at moderate to high pressures (Fridman & Kennedy 2011). The characteristic time scale of bulk recombination is $t_r = [k_{r,0}(n_0^-)^2]^{-1}$, where $k_{r,0} = A_r(T_0^-)^{b_r}$ is the typical value of the recombination rate constant. In equilibrium, the production and depletion rates of electrons are equal, $t_i = t_r$. In this limit, the ionization degree in the plasma is of order $\alpha = n_0^-/n_0 = [k_{i,0} m/(\rho_0 k_{r,0})]^{1/2} \ll 1$, with $\alpha = O(10^{-3})$ in this study, where $n_0 = \rho_0/m$. In this limit, the effects of the heat released by the chemical reactions on the plasma dynamics are negligible.

A quasi electron-neutral plasma is assumed in this investigation, in that the uncompensated charge $n^+ - n^-$ is small compared with the charge of either sign, n^+ or n^-, so that a single number density for the charged particles can simply be represented by the symbol n^-. This assumption is justified on the basis that the collisional charge-relaxation

Time scale	Description	Estimate (s)
Fast time scales:		
$t_q = t_p^2/t_c^-$	collisional charge-relaxation time scale	10^{-14}
$t_\ell = 2\pi/\omega_\ell$	incident light wave-period	10^{-13}
$t_p = 2\pi/\omega_p^-$	plasma-oscillation period	10^{-12}
$t_c^- = 1/\mathcal{V}_0^-$	e^- - heavy particles collision time scale	10^{-11}
$t_0 = R/c_0$	light propagation time scale	10^{-10}
$t_b^- = 2\pi/\omega_c^-$	e^- cyclotron-oscillation period	10^{-8}
$t_{\rm IN} = 2\pi/\omega_{\rm IN}$	electromagnetic-induction period	10^{-7}
Time scales of the plasma bulk motion:		
$t_e^- = \dfrac{\alpha\mathcal{T}t_e(\gamma-1)}{(\gamma^- - 1)}$	time scale of energy transfer to e^-	10^{-6}
$t_t^- = \dfrac{t_c^-(1+\mathcal{T})}{3\mathcal{M}(\gamma^- - 1)}$	time scale of e^- thermal relaxation	10^{-6}
$t_T^- = (\delta R)^2/D_{T,0}^-$	heat diffusion of e^- through the skin region	10^{-5}
$t_i = \dfrac{m}{A_i \mathrm{e}^{-T_{A,i}/T_0^-}\rho_0}$	ionization time scale	10^{-4}
$t_e = \dfrac{2p_0\pi\delta R^2 L}{\dot{W}_{\rm IN}(\gamma-1)}$	time scale of energy transfer to plasma	10^{-3}
$t_{mb} = \dfrac{t_{\rm IN}(t_b^-)^2}{\alpha\mathcal{M}t_c^- t_\nu}$	time scale of momentum transfer to plasma (by Lorentz force)	10^{-3}
$t_{mg} = \left(\dfrac{t_g}{t_\nu}\right)^2 \left(\dfrac{\gamma}{\mathrm{Pr}}\right) t_e$	time scale of momentum transfer to plasma (by gravity force)	10^{-2}
$t_g = (\delta R/g)^{1/2}$	gravity (ballistic time)	10^{-2}
$t_a = (\delta R)^2/D_0^a$	ambipolar diffusion time through the skin region	10^{-2}
$t_\nu = (\delta R)^2/\nu_0$	viscous diffusion of plasma through the skin region	10^{-2}
$t_T = (\delta R)^2/D_{T,0}$	heat diffusion of plasma through the skin region	10^{-2}

TABLE 2. Characteristic time scales and their estimates based on an inductively-coupled Argon plasma sustained by a homogeneous discharge at a $\omega_{\rm IN}/2\pi = 10$ MHz in a cylinder of radius $R = 0.1$ m and length $L = 0.2$ m. The adiabatic coefficients are $\gamma = \gamma^- = 5/3$. The electric power, pressure, and temperature are: $\dot{W}_{\rm IN} = 40$ kW, $p_0 = 2.2$ bar, and $T_0 = 6900$ K, respectively. In these conditions, the orders of magnitude of the AC electric field, plasma conductivity, electron temperature, ambipolar diffusion, and electron density are, respectively, $E_{\rm IN} = 100$ V/m, $\sigma_0 = 100$ ohm^{-1}m^{-1}, $T_0^- = 1$ eV, $D_0^a = 10^{-3}$ m^{2}s^{-1}, and $n_0^- = 10^{20}$ m^{-3}. The characteristic values of the collision frequencies are obtained by evaluating the expressions $\mathcal{V}^- = 1.51\cdot 10^{16}\rho[0.514 + 5.51T^- + 22.90(T^-)^2 - 6.42(T^-)^3 + 0.6(T^-)^4]$ and $\mathcal{V}^+ = \rho\sigma_t^+ v_t/m$ (Bukowski & Graves 1996) at the characteristic values ρ_0, T_0, and T_0^-, with the electron temperature in eV. Here $\sigma_t^+ = 50\mathring{A}$ is the velocity-averaged $\mathrm{Ar} - \mathrm{Ar}^+$ collision cross-section, and $v_t = [8k_{\rm B}T/(\pi m)]^{1/2}$ is the mean thermal velocity in the plasma.

time, $t_q = t_p^2/t_c^- = \epsilon_0/\sigma_0$, is much smaller than the time scales associated with the bulk motion, with $t_p = 1/\omega_p$ being the plasma response time. A breakdown of this quasineutral approximation occurs in thin Debye layers of thickness $\ell_D = (\epsilon_0 k_{\text{B}} T_0^-/n_0^- e^2)^{1/2}$, within which net electric charge develops, with $\ell_D/R = O(10^{-5}) \ll 1$ in this analysis.

During an induction cycle, the incident electromagnetic field diffuses in the conducting plasma up to distances of the same order as the characteristic skin depth δR, where δ is given by

$$\delta = \sqrt{\frac{t_{\text{IN}} t_q}{2\pi t_0^2}} = \sqrt{\frac{\epsilon_0 c_0^2}{\sigma_0 \omega_{\text{IN}} R^2}}, \tag{3.2}$$

as obtained by combining the Faraday and Ampère laws and balancing the diffusion and local accumulation of electric field. In Eq. (3.2), $t_0 = R/c_0$ is the propagation time of a ray of light across the chamber, and c_0 is the speed of light in vacuum. In principle, δ decreases with decreasing pressures, and with increasing power and chamber size, with $\delta = O(0.1)$ in this analysis.

3.2. *Thermalization and energy-transfer scales*

Because of the high collision rates, the dynamics of the plasma is characterized here using a single-velocity, two-temperature description. Similar descriptions have been successfully used in the past for inductively-coupled plasmas (Mitchner & Kruger 1973; Magin 2004). That the single-velocity description is suitable for this plasma can be understood by noticing that the momentum relaxation time of electrons, t_c^-, is very short compared to the time scales of the plasma bulk motion. Conversely, the electric power released in the plasma, $\dot{W}_{\text{IN}}$, is mainly received by the electrons, which, because of their lightness, are incapable of promptly transferring their thermal energy to the neutrals through collisions. This effect leads to long thermal relaxation times t_t^- in the electron gas. Here t_t^- is a quantity that is introduced below and is much larger than t_c^-. Nonetheless, some of the deposited energy $\dot{W}_{\text{IN}}$ is transferred to the plasma through collisions between electrons and neutrals in time scales of order $t_e = 2p_0\pi L\delta R^2/[\dot{W}_{\text{IN}}(\gamma - 1)]$, which is obtained from a balance between the unsteady and energy-deposition terms in the plasma energy equation. Specifically, the ratio of the heat-conduction time through the skin depth $t_{\scriptscriptstyle T}$ to the energy-transfer time t_e in the plasma is denoted by the dimensionless parameter

$$\Theta = \frac{t_{\scriptscriptstyle T}}{t_e} = \frac{\dot{W}_{\text{IN}}(\gamma - 1)\delta}{2\pi L D_{\scriptscriptstyle T,0} p_0}, \tag{3.3}$$

with $\Theta = O(1)$ in this analysis. If Θ was small, then the plasma could not be sustained since all the energy deposited would rapidly be dissipated through heat conduction.

The thermal energy of the electron gas rises in a much shorter time scale of order $t_e^- = \alpha(1 + \mathcal{T})t_e(\gamma - 1)/(\gamma^- - 1) \ll t_e$, which is obtained from a balance between the unsteady and energy-deposition terms in the electron energy equation. Here $\mathcal{T} = (T_0^- - T_0)/T_0 = t_t^-/t_e^-$ is a thermalization parameter that represents the dimensionless difference of electron to plasma temperatures, and which is set by the balance between the rate of energy loss by elastic collisions and the gain of thermal energy due to Ohmic heating in the electron gas. In this formulation, t_t^- is the thermal-relaxation time of the electrons $t_t^- = t_c^-(1 + \mathcal{T})/[3\mathcal{M}(\gamma^- - 1)]$, which is obtained from a balance between unsteady and elastic collision terms in the electron energy equation. The thermalization parameter $\mathcal{T}$ is treated as an order-unity quantity in this study. However, $\mathcal{T}$ becomes increasingly smaller for increasing powers and pressures, and for decreasing chamber

size, thereby indicating that the need of a two-temperature description may become less relevant in practical regimes.

The ratio of the heat conduction time $t_{\mathcal{T}}^- = (\delta R)^2/D_{\mathcal{T},0}^-$ to the energy-transfer time t_e^- in the electron gas is denoted as

$$\Theta^- = \frac{t_{\mathcal{T}}^-}{t_e^-} = \frac{\mathrm{Pr}^-\,\Theta(\gamma^- - 1)}{\mathrm{Pr}\,\alpha(1+\mathcal{T})(\gamma-1)}, \tag{3.4}$$

where $\mathrm{Pr}^- = \nu_0/D_{\mathcal{T},0}^-$ is a Prandtl number based on the characteristic electron thermal diffusivity $D_{\mathcal{T},0}^-$. It is worth emphasizing that the Prandtl number Pr^- is a small number, $\mathrm{Pr}^- = 6.8 \cdot 10^{-4}$, which indicates that the heat of the electron gas diffuses fast in the chamber due to the large values of the electron diffusivity $D_{\mathcal{T},0}^-$.

3.3. *Diffusion scales*

The diffusion of charged particles is driven by gradients of their concentrations. In the ambipolar approximation (Mitchner & Kruger 1973), the charged particles diffuse cohesively with a collision-dominated electromigration velocity of order $V_0^- = D_0^a/\delta R$, where $D_0^a = \mathscr{Z}_0^+ k_{\mathrm{B}} T_0^-/e$ is the characteristic ambipolar diffusion coefficient. Here $\mathscr{Z}_0^+ = e t_c^- \mathcal{M}^{1/2}/m^-$ is the typical value of the mobility of the ions, which limits the diffusion process for being much smaller than the mobility of the electrons by a factor of order $\mathcal{M}^{1/2} \ll 1$. The ratio of ambipolar $t_a = (\delta R)^2/D_0^a$ and ionization t_i time scales represents the Damköhler number,

$$\mathrm{Da} = \frac{t_a}{t_i} = \frac{A_i \rho_0 \delta^2 R^2 \exp(-T_{A,i}/T_0^-)}{m D_0^a}, \tag{3.5}$$

which attains a value of $O(10)$ in the present study.

3.4. *Momentum-transfer scales*

The motion of the charged particles and the thermal energy transfer to the neutrals induce bulk motion of the plasma. Two main nondimensional parameters arise from these interactions, as depicted in Figure 3 and as described below.

The gravitational force acts on the plasma as follows. The electric energy from the coil leads to temperature variations in the plasma of order $\Delta T/T_0 = O(\Theta/\gamma)$ with respect to the wall temperature, as indicated by a balance between heat conduction and power deposition in the plasma energy equation. Temperature variations are related to density variations through the equation of state, namely, $\Delta\rho/\rho_0 \sim \Delta T/T_0$. In the presence of gravitational acceleration, these thermal-expansion effects lead to forces of order $F_g = g\Delta\rho$ per unit volume in the plasma. The plasma Rayleigh number,

$$\mathrm{Ra} = \frac{t_\nu}{t_{mg}} = \frac{\dot{W}_{\mathrm{IN}} g(\gamma-1)\delta^4 R^3}{2\pi L \gamma p_0 D_{\mathcal{T},0} \nu_0^2}, \tag{3.6}$$

represents the ratio of F_g to the characteristic viscous force $\rho_0\nu_0^2/(\delta R)^3$, or equivalently, the ratio of the viscous time scale t_ν to the gravitational momentum-transfer time $t_{mg} = (\gamma/\mathrm{Pr})(t_g/t_\nu)^2 t_e$, with $t_g = (\delta R/g)^{1/2}$ being the ballistic time. The onset of gravity-driven thermal convection is sketched in Figure 2(a). In particular, circulatory motions appear for $\mathrm{Ra} \gtrsim O(1)$. In this regime, the characteristic diffusion time across the skin layer t_ν is much larger than the gravitational momentum-transfer time to the plasma in that region t_{mg}. This effect creates a buoyancy-driven boundary-layer flow along the side walls.

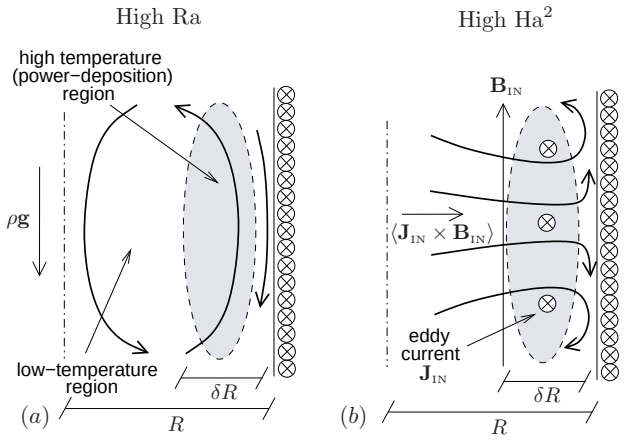

FIGURE 3. Sketches of (a) thermal-convection and (b) mean-gyrokinetic mechanisms of plasma destabilization in the lens. Thick solid arrows and dot-dashed lines indicate, respectively, flow patterns and the axis of symmetry of the lens.

Similarly, the cycle-averaged Lorentz force tends to destabilize the plasma as follows. Although the electric and magnetic fields induced by the coil have zero mean values, the average over an induction cycle of the Lorentz force has a non-zero mean. The Hartmann number,

$$\mathrm{Ha} = \sqrt{\frac{t_\nu}{t_{mb}}} = \sqrt{\frac{\dot{W}_{\text{IN}}\delta}{2\omega_{\text{IN}}\pi L\rho_0\nu_0^2}}, \tag{3.7}$$

corresponds to the square root of the ratio of the Lorentz $F_b = \sigma_0 E_{\text{IN}} B_{\text{IN}}$ and viscous characteristic forces, or equivalently, to the square root of the ratio of the viscous time scale t_ν to the electromagnetic momentum-transfer time $t_{mb} = [(t_b^-)^2 t_{\text{IN}}]/(4\pi^3\alpha\mathcal{M}t_c^- t_\nu)$. The cycle-averaged Lorentz force represents a mean ponderomotive effect that results from the net drift of all electron gyrokinetic motions induced by the incident magnetic field. In this study, the cumulative effect is important in driving the circulatory flows in the plasma, in that the diffusion time across the skin layer is shorter than the electromagnetic momentum-transfer time in that region, as sketched in Figure 3(b). Both parameters Ra and Ha become increasingly large as the electric power increases, thereby making the plasma more susceptible to instabilities.

It is worth emphasizing that the electromagnetic force, which is predominantly directed in the radial outwards direction, interacts close to the wall with the buoyancy-driven boundary-layer flow in a manner which is reminiscent of the Görtler instability of boundary layers on concave plates (Schlichting 1960), in which the pressure gradient normal to the wall induces a secondary flow in the same direction for sufficiently large curvatures or thick boundary layers. Here the effective Görtler number is proportional to $\mathrm{Ha}^2/\mathrm{Ra}$, which in the present simulations reaches values of $O(100)$, thereby indicating that the centrifugal effect caused by the electromagnetic force is dominant, as confirmed by the numerical simulations shown below. In fact, in the asymptotic limit $\delta \ll 1$, a two-dimensional problem, independent of the chamber radius, can be formulated in cartesian coordinates centered on the cylinder wall to analyze the hydrodynamic stability of the plasma boundary layer, but such analysis is not pursued in this report.

3.5. *Optical scales*

Consider a monochromatic incident plane wave of light, which enters in the plasma through the lower cylinder circular side and propagates in the positive z direction, as depicted in Figure 2. The ratio of the period of the incident wave, $t_\ell = 2\pi/\omega_\ell$, to the plasma response time, t_p, is related to the effective relative permittivity of the plasma ϵ_p as

$$\Lambda = 1 - \epsilon_p = (t_\ell/t_p)^2. \tag{3.8}$$

In order to avoid shielding of radiation, dissipation of the wave energy, and presence of the focal point inside the lens, in this study ϵ_p is set to attain values smaller than unity but not too small, as suggested in Figure 1. In this way, the incident wave frequency ω_ℓ is typically restricted to the THz regime or higher, resulting in wavelengths $\lambda_\ell = c_0 t_\ell$ in the submillimeter range. In this limit, t_ℓ is also much shorter than the collision time t_c^-, and variations in the index of refraction n can be estimated as $n - 1 = O(\Lambda)$, with $\Lambda \lesssim O(10^{-1})$, thereby inducing ray bending and phase distortion as the light beam propagates across the lens. The characteristic bending angle of the rays due to refraction, which is of order Λ, is small in the lens. The resulting order of magnitude of the dimensionless steady optical path difference is $\mathrm{OPD}/L = O(\Lambda)$. The characteristic focal length normalized with the cylinder size can be estimated as $\mathcal{F} = f/(2R) \sim 1/(s\Lambda)$ by comparing the plasma and thin-lens phase-transmission functions, where $s = L/2R$ is the lens aspect ratio.

It is of some interest to compare the characteristic refractive-index variations $n - 1 = O(\Lambda)$ achieved by using this plasma lens to the corresponding variations that can be obtained by employing temperature differences in gas lenses (Michaelis *et al.* 2013), which are of order $n - 1 = O(K_{GD}\Delta T/T)$, with $K_{\mathrm{GD}} = 2.8 \cdot 10^{-4}$ being the Gladstone-Dale coefficient. In idealized conditions, and for temperature differences $\Delta T/T$ of order unity, the plasma lens outperforms the focal power of gas lenses by a factor of order $\Lambda/K_{GD} \gg 1$, which reaches values of order 10^2 in the present simulations. In general, thermal effects on the index of refraction are of secondary importance as long as the electron density in the plasma remains much larger than the characteristic value $\varepsilon_0 m^- \omega_\ell^2 K_{\mathrm{GD}}/e^2$, this threshold density being of order $O(10^{18})$ m^{-3} in the present study. However, according to this study, the high powers and the corresponding induced flows in the plasma may cause departures from the axisymmetry implied in the above estimates and an overall degradation of the plasma lens.

4. Conservation equations

The plasma conservation equations are formulated in the framework of a low Mach-number approximation, in which the thermodynamic chamber pressure p is uniform in space but is allowed to vary in time. The corresponding dynamic pressure is denoted by the symbol Π.

Using the scales introduced in the previous section, the dimensionless variables

$$t' = \frac{t}{t_\nu}, \quad \mathbf{x}' = \frac{\mathbf{x}}{\delta R}, \quad \mathbf{v}' = \frac{\mathbf{v}' t_\nu}{\delta R}, \quad \rho' = \frac{\rho}{\rho_0}, \quad \Pi' = \frac{\Pi t_\nu^2}{\rho_0 (\delta R)^2}, \quad p' = \frac{p}{p_0}, \quad T' = \frac{T}{T_0},$$

$$n^{-\prime} = \frac{n^-}{n_0^-}, \quad T^{-\prime} = \frac{T^-}{T_0^-}, \quad \mathbf{V}^{-\prime} = \frac{\mathbf{V}^-}{V_0^-}, \quad \mathbf{J}_{\mathrm{IN}}{}' = \frac{\mathbf{J}_{\mathrm{IN}}}{\sigma_0 E_{\mathrm{IN}}}, \quad \mathbf{E}_{\mathrm{IN}}{}' = \frac{\mathbf{E}_{\mathrm{IN}}}{E_{\mathrm{IN}}}, \quad \sigma' = \frac{\sigma}{\sigma_0},$$

Parameter	Description	Value (-)
$\mathrm{Ra} = \dfrac{t_\nu}{t_{mg}} = \dfrac{\dot{W}_{\mathrm{IN}} g(\gamma-1)\delta^4 R^3}{2\pi L\gamma p_0 D_{T,0}\nu_0^2}$	plasma Rayleigh number	0.2
$\mathrm{Ha} = \sqrt{\dfrac{t_\nu}{t_{mb}}} = \sqrt{\dfrac{\dot{W}_{\mathrm{IN}}\delta}{2\omega_{\mathrm{IN}}\pi L\rho_0\nu_0^2}}$	Hartmann number	5.7
$\mathrm{Da} = \dfrac{t_a}{t_i} = \dfrac{A_i\rho_0(\delta R)^2 \mathrm{e}^{-T_{A,i}/T_0^-}}{mD_0^a}$	Damköhler number	61.5
$\Theta = \dfrac{t_T}{t_e} = \dfrac{\dot{W}_{\mathrm{IN}}(\gamma-1)\,\mathrm{Pr}}{2\pi L p_0 D_{T,0}}$	plasma energy-transfer parameter	1.4
$\Theta^- = \dfrac{t_T^-}{t_e^-} = \dfrac{\mathrm{Pr}^-\,\Theta(\gamma^- - 1)}{\mathrm{Pr}\,\alpha(1+\mathcal{T})(\gamma-1)}$	e^- energy-transfer parameter	2.2
$\mathrm{Pr} = \dfrac{t_T}{t_\nu} = \dfrac{\nu_0}{D_{T,0}}$	plasma Prandtl number	0.7
$\mathrm{Pr}^- = \dfrac{t_T^-}{t_\nu} = \dfrac{\nu_0}{D_{T,0}^-}$	e^- Prandtl number	$6.8\cdot10^{-4}$
$\mathrm{Le}^a = \dfrac{t_a}{t_T} = \dfrac{D_{T,0}}{D_0^a}$	Lewis number (ambipolar)	0.3
$\delta = \sqrt{\dfrac{t_{\mathrm{IN}} t_q}{2\pi t_0^2}} = \sqrt{\dfrac{\epsilon_0 c_0^2}{\sigma_0\omega_{\mathrm{IN}} R^2}}$	nondimensional skin depth	0.05
$\mathcal{T} = \dfrac{t_t^-}{t_e^-} = \dfrac{T_0^- - T_0}{T_0}$	plasma thermalization parameter	0.6
$\alpha = \dfrac{n_0^- m}{\rho_0}$	ionization degree	$4.1\cdot10^{-4}$
$\Lambda = \left(\dfrac{t_\ell}{t_p}\right)^2$	characteristic refractive-index variation	0.25
$\mathcal{F} = \dfrac{f}{2R}$	lens nominal F-number	4.0
$\beta_i = \dfrac{T_{A,i}}{T_0^-}$	nondimensional activation temperature	18.9
$s = \dfrac{L}{2R}$	lens aspect ratio	1.0
$\mathcal{M} = \dfrac{m^-}{m}$	electron-to-neutral mass ratio	$1.4\cdot10^{-5}$
$\theta_w = \dfrac{T_w}{T_0}$	nondimensional wall temperature	0.04

TABLE 3. Characteristic dimensionless parameters and their values in the present simulations. The operating conditions are described in the caption of Table 2.

$$\mathbf{B}_{\mathrm{IN}}{}' = \frac{\mathbf{B}_{\mathrm{IN}}}{B_{\mathrm{IN}}}, \quad \mu' = \frac{\mu}{\mu_0}, \quad \kappa' = \frac{\kappa}{\kappa_0}, \quad \kappa^{-\prime} = \frac{\kappa^-}{\kappa_0^-}, \quad \mathcal{V}^{-\prime} = \frac{\mathcal{V}^-}{\mathcal{V}_0^-}, \quad \mathcal{V}^{+\prime} = \frac{\mathcal{V}^+}{\mathcal{V}_0^+}, \tag{4.1}$$

are utilized in this section. The primes used to denote dimensionless variables in (4.1) are dropped in what follows. In these variables, the mass, momentum, and thermal-energy

conservation equations for the plasma become

$$\frac{\partial \rho}{\partial t} + \nabla \cdot (\rho \mathbf{v}) = 0, \tag{4.2}$$

$$\frac{\partial \rho \mathbf{v}}{\partial t} + \nabla \cdot (\rho \mathbf{v}\mathbf{v}) = -\nabla \Pi + \nabla \cdot \boldsymbol{\tau} - \mathrm{Ra}\Delta\rho \mathbf{e_z} + \mathrm{Ha}^2 \langle \mathbf{J}_{\mathrm{IN}} \times \mathbf{B}_{\mathrm{IN}} \rangle, \tag{4.3}$$

$$\frac{\partial}{\partial t}(\rho T) + \gamma \nabla \cdot (\rho \mathbf{v} T) = \frac{\gamma \nabla \cdot (\kappa \nabla T)}{\mathrm{Pr}} + \frac{\Theta \langle \mathbf{J}_{\mathrm{IN}} \cdot \mathbf{E}_{\mathrm{IN}} \rangle}{\mathrm{Pr}}. \tag{4.4}$$

In addition, the equation of state

$$p(t) = \rho T \tag{4.5}$$

is used to obtain the thermodynamic pressure in the plasma. Similarly, $\boldsymbol{\tau} = \mu[(\nabla \mathbf{v} + \nabla \mathbf{v}^T) - 2(\nabla \cdot \mathbf{v})\boldsymbol{I}/3]$ represents the viscous stress tensor, where $\boldsymbol{I}$ is the identity tensor and μ is a temperature-dependent dynamic viscosity that is introduced below.

The nondimensional species and thermal-energy conservation equations for the electrons in the nondimensional variables (4.1) are

$$\frac{\partial n^-}{\partial t} + \nabla \cdot (n^- \mathbf{v}) = -\frac{\nabla \cdot (n^- \mathbf{V}^-)}{\mathrm{Le}^a \, \mathrm{Pr}} + \frac{\mathrm{Da}}{\mathrm{Le}^a \, \mathrm{Pr}} \left[k_i \rho n^- - k_r (n^-)^3 \right], \tag{4.6}$$

$$\frac{\partial}{\partial t}(n^- T^-) = \frac{\gamma^- \nabla \cdot (\kappa^- \nabla T^-)}{\mathrm{Pr}^-} + \frac{\Theta^-}{\mathrm{Pr}^-} \left[\langle \mathbf{J}_{\mathrm{IN}} \cdot \mathbf{E}_{\mathrm{IN}} \rangle - n^- \mathcal{V}^- \frac{(1+\mathcal{T})}{\mathcal{T}} \left(T^- - \frac{T}{1+\mathcal{T}} \right) \right]. \tag{4.7}$$

In this formulation, Ra, Ha, Da, Θ, Θ^-, Le^a and Pr and Pr^- are dimensionless parameters given in Table 3. Additionally, $\mathcal{V}^-$ is the collision frequency of electrons against neutrals nondimensionalized with its characteristic value $\mathcal{V}_0$.

In Eq. (4.6), the diffusion velocity $\mathbf{V}^-$ is calculated from the expression

$$n^- \mathbf{V}^- = -\frac{\nabla (n^- T^-)}{\mathcal{V}^+}, \tag{4.8}$$

where use of the ambipolar approximation for unmagnetized diffusion has been made (Mitchner & Kruger 1973). Here $\mathcal{V}^+$ is the frequency of collisions of ions against neutrals nondimensionalized with its characteristic value $\mathcal{V}_0^+$. Note that the collision frequencies $\mathcal{V}^+$ and $\mathcal{V}^-$ depend on pressure and local temperatures of plasma and electrons through the dimensionless versions of the expressions given in the caption of Table 2. Additionally, k_{1f} and k_{1b} are the dimensionless rates of ionization and recombination, namely

$$k_i = \exp\left[\beta_i \left(\frac{T^- - 1}{T^-} \right) \right], \quad k_r = (T^-)^{b_2}, \tag{4.9}$$

where b_2 and β_i are given in Tables 1 and 3, respectively.

Equations (4.2)-(4.4) and (4.6)-(4.7) are integrated subject to the boundary conditions

$$\mathbf{v} = 0, \quad T - \theta_w = n^- = 0, \tag{4.10}$$

on the walls, where θ_w is the wall temperature normalized with T_0, and $s = L/2R$ is the lens aspect ratio. Specifically, the boundary condition used here for the electron-number density n^-, namely, $n^- = 0$, corresponds to a perfectly catalytic wall.

The dimensionless molecular viscosity μ and thermal conductivity κ of the plasma are calculated from the presumed power-law dependence $\mu = \kappa = T^c$, where $c = 0.7$. Results from the monoatomic gas-kinetic theory (Vincenti & Kruger 1965) are used to

approximate the dimensionless thermal conductivity of the electrons as $\kappa^- = n^- T^- / \mathcal{V}^-$. Additionally, the adiabatic coefficients of the plasma and electron gases are assumed to be constants and equal to $\gamma^- = \gamma = 5/3$. More involved and rigorous formulations, which are beyond the scope of this study, are available for calculating plasma transport coefficients (see, for instance, Magin & Degrez (2004)). Such extended transport treatments, as well as plasma-discharge complex chemistry, may be needed if detailed comparisons with experiments are pursued.

4.1. *Propagation of the incident electromagnetic field*

In Eqs. (4.3), (4.4) and (4.7), the incident electromagnetic wave is obtained as follows. Combination of the Faraday and Ampère laws in the Maxwell equations leads to the dimensionless Helmholtz problem

$$\nabla_\theta^2 \mathcal{E}_{\theta,\text{IN}} = j\sigma \mathcal{E}_{\theta,\text{IN}} \tag{4.11}$$

for the phasor of the electric field $\mathcal{E}_{\theta,\text{IN}}$, with ∇_θ^2 being the azimuthal component of the vector Laplacian in cylindrical coordinates. Here only the azimuthal component of the electric field is considered, although this component can depend on the three spatial coordinates, $\mathcal{E}_{\theta,\text{IN}} = \mathcal{E}_{\theta,\text{IN}}(r,\theta,z)$. Specifically, the oscillatory electric field is represented in complex form by $\mathbf{E}_{\text{IN}} = \mathscr{R}e\{\mathcal{E}_{\theta,\text{IN}} \mathrm{e}^{j2\pi\omega t}\}\mathbf{e}_\theta$, where j is the imaginary unit, $\mathbf{e}_\theta$ is a unit vector in the azimuth direction, and $\omega = t_\nu / t_{\text{IN}}$ is a scaling factor that arises from the nondimensionalization of the time coordinate with t_ν in (4.1). In this formulation, σ is the dimensionless electric conductivity calculated from the expression

$$\sigma = n^- / \mathcal{V}^-, \tag{4.12}$$

which is appropriate for this collision-dominated plasma. Three important additional assumptions have been made in order to derive Eq. (4.11). First, the incident current density has been obtained from the Ohm's law,

$$\mathcal{J}_{\theta,\text{IN}} = \sigma \mathcal{E}_{\theta,\text{IN}}, \tag{4.13}$$

in which the Hall conductivity has been neglected since $t_c^- \ll t_b^-$ in this plasma. Second, the electric conductivity has been assumed to vary in much longer time scales than t_{IN}, an approximation justified on the basis that the electron density and temperature fields vary on longer (drift) time scales imposed by flow gradients according to equations (4.2)-(4.7). Lastly, the displacement current has been neglected since the characteristic size of the chamber is much smaller than the wavelength of the incident electromagnetic wave from the coil, $\omega_{\text{IN}} R / c_0 = O(t_0 / t_{\text{IN}}) \ll 1$.

The phasor of the incident magnetic field, $\mathcal{B}_{\text{IN}}$, can be calculated from the spatial distribution of $\mathcal{E}_{\theta,\text{IN}}$ using the Faraday's law, namely

$$\mathcal{B}_{\text{IN}} = j\nabla \times (\mathcal{E}_{\theta,\text{IN}} \mathbf{e}_\theta), \tag{4.14}$$

where $\nabla\times$ is the curl in cylindrical coordinates. In particular, $\mathcal{B}_{\text{IN}}$ has axial and radial components, the latter arising as a result of spatial variations of the electric field in the axial direction by, for instance, the indirect effect of gravity in the electron-density distribution.

By computing the solution to (4.11) and using expressions (4.13) and (4.14), the sources in the conservation equations (4.3), (4.4), and (4.7) can be calculated as

$$\langle \mathbf{J}_{\text{IN}} \cdot \mathbf{E}_{\text{IN}} \rangle = \frac{\sigma}{2} \mathcal{E}_{\theta,\text{IN}} \mathcal{E}_{\theta,\text{IN}}^\star \quad \text{and} \quad \langle \mathbf{J}_{\text{IN}} \times \mathbf{B}_{\text{IN}} \rangle = \frac{\sigma}{2} \mathscr{R}e\left\{ \mathcal{E}_{\theta,\text{IN}} \mathrm{e}_\theta \times \mathcal{B}_{\text{IN}}^\star \right\}, \tag{4.15}$$

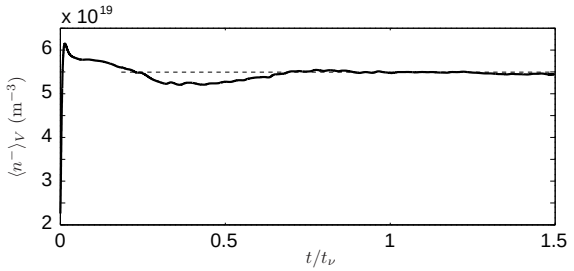

FIGURE 4. Time evolution of the dimensional volume-averaged electron density.

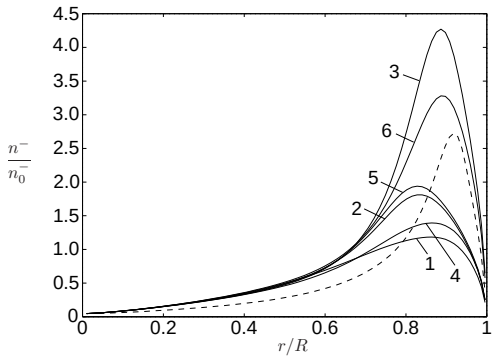

FIGURE 5. Instantaneous radial profiles of electron density at the cylinder mid-axial location and $t/t_\nu = 1.5$ for different consecutive values of the azimuthal angle θ spaced 15° apart (solid lines 1-6). The figure also shows the electron-density distribution averaged in axial and azimuthal directions (dashed line).

which represent, respectively, the induction-cycle averages of the dimensionless Ohmic power dissipation and the Lorentz force, both quantities being measured per unit volume. In this formulation, the superindex * refers to complex-conjugate quantities.

Equation (4.11) is integrated simultaneously with Eqs. (4.2)-(4.4) and (4.6)-(4.7), subject to the boundary conditions $\mathcal{E}_{\theta,\mathrm{IN}} = C$ on the side walls, and $\partial\mathcal{E}_{\theta,\mathrm{IN}}/\partial z = 0$ on the top and bottom walls. Here, C is a real constant obtained by the constraint that the electric power dissipated in the plasma is equal to $\dot{W}_{\mathrm{IN}}$.

5. Development of three-dimensional unsteady plasma flows in the lens

The conservation equations and boundary conditions described in the previous section are integrated numerically in what follows. The numerical integration is advanced in time using an explicit Adams-Bashforth scheme, except for the diffusion terms which are advanced employing an implicit Crank-Nicholson technique to overcome the stringent time-step requirements due to the vanishing mesh size in the azimuthal direction close to the axis. A three-dimensional structured computational mesh stretched towards the side walls is utilized. The spatial disctretization follows a second-order central-differences scheme. The Poisson and Helmholtz equations for the dynamic pressure and electric field, respectively, are solved using a biconjugate method with algebraic multigrid preconditioning. Simulation data for analysis are collected at snapshots after the transient period,

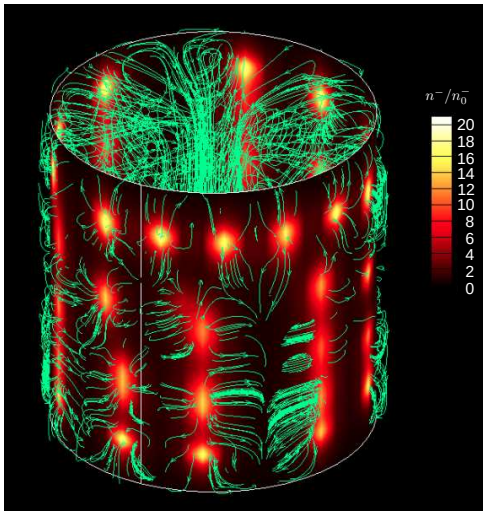

FIGURE 6. Instantaneous snapshot of the dimensionless electron-density distribution close to the wall within the skin region (solid contours), together with flow streamlines (green lines, color online).

when the main volume-averaged plasma variables have reached quasi-steady values and the effects of the initial conditions are expected to be minimal, as depicted in Figure 4.

In these operating conditions, plasma destabilization is first observed in Figure 5, which reveals noticeable differences between local and spatially averaged electron densities. Further inspection of the three-dimensional plasma dynamics is performed in Figure 6, which shows localized electron-rich spots in the plasma skin region and streamlines flowing through the center of these zones in a way similar to the dynamics sketched in Figure 3(b). In particular, unsteady complex flow structures develop in the plasma bulk, as evidenced by the contorted streamlines in Figure 6. Low-dimensional projections of these streamlines along an axial plane are shown in Figure 7. The cycle-averaged Lorentz force displaces plasma towards the wall in electron-rich regions, as shown in Figure 7(a). Similarly, these regions are typically hot and are located close to the cold wall, as observed in Figure 7(b). The corresponding temperature gradient produces a buoyancy-driven flow that has a lower intensity than the flow induced by the electromagnetic forces, as indicated in Tables 2 and 3 by the relatively shorter electromagnetic momentum-transfer time scale t_{mb} (in comparison with the gravitational momentum-transfer time scale t_{mg}), and by the large value of the Hartmann number squared Ha^2 (in comparison with the Rayleigh number Ra). Further investigations are warranted to study these fundamental hydrodynamic-stability phenomena in plasmas.

The isolated electron-rich regions observed in Figures 6 and 7 represent strong departures from axisymmetry, which degrade the optical performance of the lens, as shown in the following section.

6. Optical performance of the plasma lens

A monochromatic, collimated, and planar incident wave of light with frequency $\omega_\ell = 5\omega_p$ was propagated through the plasma in the axial direction from the bottom to the top sides of the lens, where $\omega_p = 0.1$ THz is the maximum value of the plasma frequency

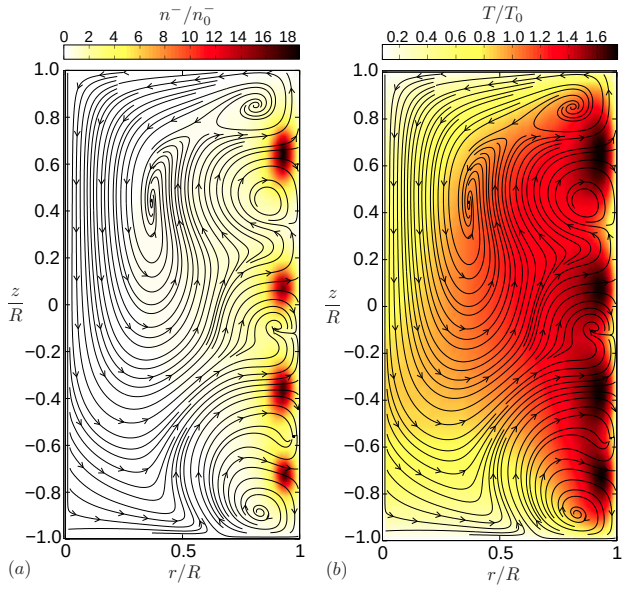

FIGURE 7. Instantaneous axial cross sections of (a) dimensionless electron-density distribution, and (b) plasma temperature. The figure also shows in-plane projected streamlines.

in these operating conditions. The corresponding incident wavelength and London length are $\lambda_\ell = 0.5$ mm and $\lambda_p = 1$ mm, respectively, which yield characteristic variations of the refractive index of order $1 - n \sim \Lambda = 0.25$.

Figure 8 shows, for the same instantaneous snapshots depicted in Figures 5-7, the dimensionless optical path difference $\mathrm{OPD}/L = \int_{-s}^{s} n dz - 1$ where the refractive index n is calculated using Eq. (2.1). In this way, the light colored regions in Figure 8 correspond to large positive values of $-\mathrm{OPD}$, which are representative of light rays propagating with increasingly large phase velocities. These rays are accelerated as they propagate through electron-rich zones. However, the lack of axisymmetry in the electron-density distribution observed in Figures 5-7 translates here into incoherent optical distortions that render the lens incapable of focusing light. In fact, a Zernike decomposition of the wavefront shown in Figure 8 reveals that only a 6% of its amplitude is suitable for focusing light, with a focal length of order $f \sim 200R$ and an effective F-number $\mathcal{F} = f/2R \sim 100$.

7. Conclusions

In this study, conditions are identified in which an inductively-coupled plasma lens becomes unstable. Analyses of the characteristic scales reveals two relevant mechanisms of momentum transfer to the plasma, namely, gravity-driven convection and cycle-averaged electromagnetic forces, whose intensities are quantified by the corresponding nondimensional parameters. These effects become more important as, for instance, the electric power of the lens increases. Three-dimensional numerical integrations reveal that the electron-density distribution develops noticeable azimuthal fluctuations as a result of the plasma flow, which, in turn, degrade the optical properties of the lens.

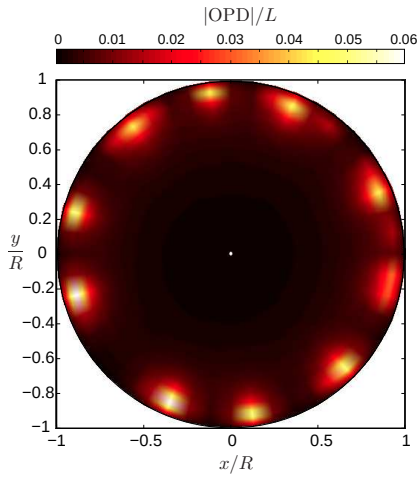

FIGURE 8. Position of the incident light wavefront relative to the mean (or, equivalently, negative OPD) after passing through the plasma lens. White and dark regions indicate fast and slow traveling rays, respectively.

Acknowledgments

This investigation was funded by DARPA, Grant # N66001-12-1-4198. The authors are grateful to Prof. Thierry Magin and Prof. Mark Capelli for useful discussions on plasma physics.

REFERENCES

BUKOWSKI, J. D. & GRAVES, D. B. 1996 Two-dimensional fluid model of an inductively coupled plasma with comparison to experimental spatial profiles. *J. Appl. Phys.* **80** (5), 2614–2623.

FRIDMAN, A. & KENNEDY, L. A. 2011 *Plasma Physics and Engineering.* CRC Press.

MICHAELIS, M. M., MAFUSIRE, C., GROBLER, J. H. & FORBES, A. 2013 Focusing light with a flame lens. *Nat. Commun.* **4**, 1869.

NEISWANDER, B. W., MATLIS, E. & CORKE, T. C. 2012*b* Plasma lens for optical path difference control. *AIAA J.* **50**, 123–129.

MAGIN, T. E. 2004 *A Model for Inductive Plasma Wind Tunnels.* Ph.D. Thesis, Université Libre de Bruxelles.

MAGIN, T. E. & DEGREZ, G. 2004 Transport properties of partially ionized and unmagnetized plasmas. *Phys. Rev. E* **70**, 046412.

MITCHNER, M. & KRUGER, C. H. 1973 *Partially Ionized Gases.* Wiley & Sons.

SCHLICHTING, H. 1960 *Boundary-Layer Theory.* Mc-Graw Hill.

STEVEFELT, J., BOULMER, J., & DELPECH, J.-F. 1975 Collisional-radiative recombination in cold plasmas. *Phys. Rev A* **12**, 1246–1251.

VINCENTI, W. G. & KRUGER, C. H. 1965 *Introduction to Physical Gasdynamics.* Kreiger Publishing Company.

WANG, M., MANI, A. & GORDEYEV, S. 2012 Physics and computation of aero-optics. *Annu. Rev. Fluid Mech.* **44**, 299–321.